Predicting urban heat island circulation using CFD

Xiaoxue Wang[*], Yuguo Li

Department of Mechanical Engineering, The University of Hong Kong, Pokfulam Road, Hong Kong

A B S T R A C T

Most existing microscale computational fluid dynamics (CFD) models and mesoscale meteorological models cannot consider multi-scale urban wind flows, as neither can completely take into account the mesoscale and microscale physics, and their interactions. Here we suggest a CFD model which has good potential for development of the meso-micro scale models for predicting and designing multi-scale urban airflows. The principal idea is to use CFD numerical methods to solve a set of governing equations with appropriate boundary conditions that can govern both major mesoscale and microscale flow characteristics. Based on the coordinate transformation method proposed by Kristóf, Rácz and Balogh (2009), we derived a similar set of governing equations with some improvements and used an existing porous turbulence model for modeling the urban canopy layer. The approach was then successfully implemented using a commercial CFD package (Fluent) for studying urban heat island circulation (UHIC), which is considered to be one of the most difficult problems in CFD. Our predicted mean quantities agree well with existing data in the literature obtained from large eddy simulations, mesoscale models, and laboratory experiments. Our predicted results also reveal the effects of the different heat fluxes and urban height of a city on UHIC characteristics.

1. Introduction

The urban climate is multi-scale in nature. The multi-scale nature of wind flows in a city may be illustrated by the phenomenon of urban heat island circulation (UHIC) [16], which occurs when the synoptic wind is weak. During the day, buildings are warmed by solar and other anthropogenic heat. A natural convection boundary layer develops along each building wall. These (microscale) thermal boundary layer flows merge either within or above the urban canopy layer. Multiple building plumes develop above the urban canopy layer. As there are tens or hundreds of thousands of buildings in a large city, there can be the same number of plumes, which again merge into a large urban plume. The air is lifted up due to the buoyancy effect, so the pressure is lower in the city center area, which drives the inward flows through the urban edges, and eventually develops into (mesoscale) urban heat island circulation when there is an inversion. As shown in Fig. 1, each individual

building plume would flow upward if the building were isolated, but in an urban setting, only those in the city center would have upward plumes, and the plumes of buildings at the edges of the city would bend towards the city center.

The urban heat island effect forms an important background to the study of the built environment. Gal and Unger [16] studied the ventilation path over large areas when UHIC occurs. The urban heat island also has significant impacts on building energy consumption and outdoor air quality [35]. Giridharan et al. [19] studied UHI intensity in a high-rise high-density environment. Ng et al. [53] also studied methods for weakening the UHI in high-rise high-density environments.

One cannot predict or design wind flows around each individual building without considering the flows of the entire city. Due to complex turbulence, accurate prediction of buoyancy-driven flows around a single building requires a few million grid points using computational fluid dynamics (CFD). For hundreds of thousands of buildings in a large city, hundreds of billions of grid points would be needed. The largest known city-scale CFD simulation for modeling urban wind flows is for a 33×33 km area of Tokyo [1] on a supercomputer using five billion grids. Such computing resources are not available to the average urban planner or building designer. The

* Corresponding author.
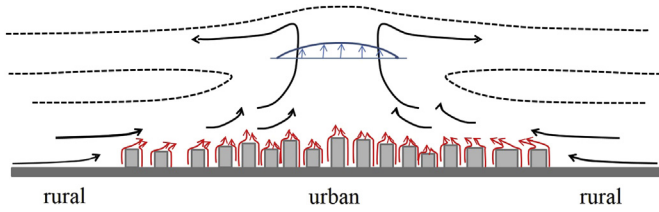*E-mail address:* xxwang@connect.hku.hk (X. Wang).

Fig. 1. An illustration of the multi-scale nature of the urban heat island circulation phenomenon.

modeling study of Ashie and Kono [1] focused on the overall city-scale flows, but their vertical extend of the computational domain is small so that the atmospheric stratification and UHIC could not be taken into account. Their flows are driven by a pre-defined wind (sea-breeze).

Modeling multi-scale urban climate is challenging. A modeling approach that has both mesoscale and microscale capabilities is ideal. It is referred to as a "meso-microscale model" by Yamada and Koike [48]; so we have adopted this term here. Both downscaling mesoscale meteorological models (MMMs) and upscaling CFD models are possible; see reviews of Yamada and Koike [36], Mochida et al [48] and Balogh and Kristóf [2]. Hybrid or joint modeling methods are also possible [40]. These reviews suggested that modeling multi-scale UHIC is an even more challenging problem. Mochida et al [36] pointed out that "*one of the significant weaknesses of the engineering CFD models is insufficient treatment of modeling the buoyancy effects on turbulent diffusion that play significant roles under calm wind conditions*". Yamada and Koike [48] suggested that "*none of the existing mesoscale meteorological models (MMMs) consider complete thermal effects of buildings (diurnal heating/cooling of building roofs/walls, shadows, and multiple reflections of long-wave radiation energy from building walls).*" In a recent review Emeis [12] wrote that coupling CFD models with MMMs "*is known to be hampered by the problem of adequately representing turbulence and thermal convection in these models either through a parameterization or by fully resolving them.*"

There are at least two major issues in modeling multi-scale UHIC. The first is a need for a properly combined mathematical model that can represent both mesoscale and microscale flows. The mesoscale flows are compressible in nature while the microscale flows are incompressible. Though the thermal effect in mesoscale flows can be modeled by appropriate parameterization of surface heat fluxes or temperature, the thermal effect in the microscale flows needs a detailed model of temperature or heat flux description on complete urban surfaces [51]. The second issue relates to the need for a robust numerical solver for handling both the mesoscale and microscale flow equations. The numerical issue is not critical, as a number of effective methods exist for all flow speeds (e.g. Ref. [34]).

Upscaling CFD models holds great potential in the development of a meso-micro scale model for the purpose of predicting and designing multi-scale urban airflows. CFD models have been successfully developed for complex building flows [4,5]. The use of finite volume methods and unstructured grids has enabled most of the complex geometry to be modeled. The principal idea is to use CFD numerical methods to solve a set of governing equations with appropriate boundary conditions that can govern both major mesoscale and microscale flow characteristics. The most successful CFD numerical methods are probably the pressure-based solvers, which are used in most existing commercial CFD software such as Fluent (ANSYS Inc, USA). The crucial component of a pressure-based solver is in the solution of the Poisson equation for pressure or pressure correction. The existing governing equations for mesoscale flows cannot be easily solved by the current pressure-based CFD solvers.

The so-called *soundproof* or anelastic equations were developed [10,30] for atmospheric flows to avoid very fine time steps. A vertical coordinate transformation, such as a terrain-following pressure coordinate is often used in mesoscale models to include atmospheric stratification without increasing instability. The terrain-following coordinate [39] is widely used in mesoscale flow codes such as WRF [41,46], but it cannot deal with a steep topography. We became interested in the new coordinate transformation proposed in Kristóf et al. [26]. The method was specifically developed for adapting pressured-based CFD models to include atmospheric stratification, anelasticity and the Coriolis force. Kristóf et al [26] concluded that "*Motivation for development of the present method came from ideas for application to urban climatology… therefore, the CFD solver will eventually be adapted to urban heat island convection problems. Although this goal is not yet fully achieved, the present method can be used with benefits, inter alia, urban air quality…in an urban atmosphere under different stability conditions*".

We revisited the coordinate transformation method proposed by Kristóf, Rácz and Balogh [26]; and refer to it as the KRB coordinate. We derived a similar set of governing equations as Kristóf et al. [26] resulting in a slight improvement. We successfully implemented the new model for studying urban heat island circulation using Fluent, a commercial CFD package. We compared our prediction with existing data in the literature obtained from large eddy simulation and mesoscale models, and with laboratory experiments. A porous turbulence model, as tested by Hang and Li [20,21], was used for modeling the entire urban canopy layer.

2. Methodologies

We essentially followed the derivation process of Kristóf et al [26]. Our derivation has allowed us to reexamine some major assumptions and identify possibly overlooked terms and interpretations of the new model.

In the mesoscale atmosphere, the basic variables of weather condition ψ are decomposed as reference state $\overline{\psi}$ in hydrostatic balance and the variation part ψ' [31].

$$\psi = \overline{\psi} + \psi' \tag{1}$$

Where $\overline{\psi}$ is the averaged-value, integrated horizontally over a large-scale, hydrostatic environment, and ψ' is the difference between the actual value and the averaged value, which evolves due to the effect of turbulence and other perturbations. We adopt the anelastic approximation in mesoscale weather forecasting to eliminate the sound waves and the need for a very fine time step. The major features of anelastic approximation are omitting of the term $\partial \rho / \partial t$ and replacing the density ρ with the reference state density [3,37].

2.1. Reference state

The reference state is the hydrostatic atmosphere [24]. The basic derivation of the reference state is shown in appendix A.

Kristof et al. [26] used a simple form of exponential Equation (2) to represent the reference state density. Comparing Equations (A3) and (A6):

$$\overline{\rho} = \rho_0 e^{-\xi z} \tag{2}$$

where ξ is the transformation coefficient, and substituting Equation (A3) with Equation (2), the transformation coefficient ξ can be determined as follows:

$$\xi = -\frac{1}{z}\left(\frac{g}{R\Gamma} - 1\right)\ln\left(\frac{T_0 - \Gamma z}{T_0}\right) \quad (3)$$

For the hydrostatic atmosphere, the variation of transformation coefficient ξ as a function of height is not significant. Kristóf et al. [26] suggested that a constant value of 10^{-4} m^{-1} can be used. They also showed that for heights below 4 km, the error in density calculation is less than 4% compared to the standard atmosphere when Equation (2) is used with constant ξ.

Kristóf et al. [26] neglected to mention that the transformation coefficient ξ also changes with different temperature lapse rates of the reference state as shown in Fig. 2. There is no need to refer to the standard atmosphere. A large absolute value of the temperature lapse rate leads to a relatively large variation of the transformation coefficient. We suggest using different transformation coefficient values for different temperature lapse rates. The change of the co-efficient for a constant temperature lapse rate is found to be less than 5% below 3000 m. Since the vertical height is less than 3000 m for most urban meso-micro flows, the average value of the coeffi-cient below this altitude is used in our study for a specific tem-perature lapse rate.

2.2. The KRB coordinate

Kristóf et al. [26] introduced a new vertical coordinate to enable simulation of mesoscale flows in a pressure-based CFD model, i.e. the KRB (Kristóf -Rácz -Balogh) coordinate. In the KRB coordinate, a KRB height h is defined and related to the reference pressure. The basic idea is that for the KRB height, the pressure gradient in the reference state in a layer of height dz and a layer of height dh should be the same. Therefore, based on the hydrostatic Equation (A5), the KRB height h is related to an increment in the original physical height z by Equation (4).

$$d\overline{p} = \overline{\rho}gdz = \rho_0 gdh \quad (4)$$

Substituting Equations (2) and (3) into Equation (4), the KRB height h can be found as a function of the both transformation coefficient ξ defined earlier and the original physical height z. The transformation coefficient ξ is taken as a constant and a function of the initial temperature lapse rate.
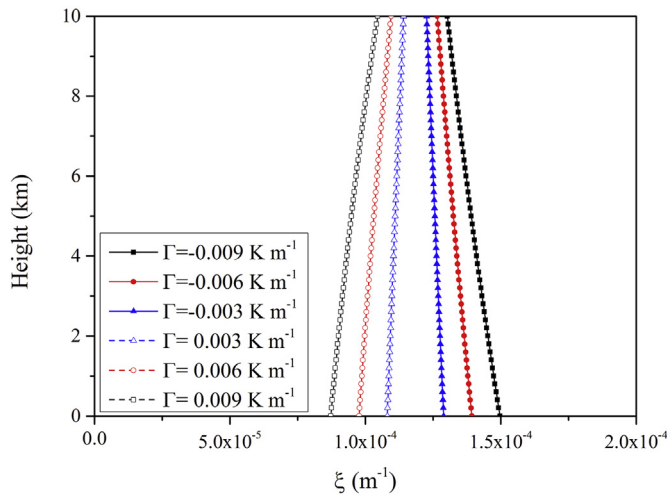
$$h = \frac{1}{\xi}\left(1 - e^{-\xi z}\right) \quad (5)$$

Directly integrating Equation (4), without the simplification of the coordinate transformation coefficient, the transformed height here can also be expressed as Equation (6), which is a density-based but height-like coordinate, referred to here as the DB (Density-Based) coordinate. The difference between the DB and KRB co-ordinates lies in the use of different transformation coefficients.

$$z_{DB} = -\frac{T_0 R}{g}\left[\left(\frac{T_0 - \Gamma z}{T_0}\right)^{\frac{g}{R\Gamma}} - 1\right] = \frac{T_0 R}{g}\left(1 - \frac{\overline{p}}{p_0}\right) \quad (6)$$

Substituting ideal gas equation ($p_0 = \rho R T_0$) in the above Equation (6), the DB coordinate is $z_{DB} = (p_0 - \overline{p})/(\rho_0 g)$. Hence the DB coor-dinate effectively compressed the atmosphere rendering it homogeneous.

The pseudo height coordinate is defined by White and Beare [44]; as shown in Equation (13)

$$z_{kap} = \frac{C_p T_0}{g}\left[1 - \left(\frac{\overline{p}}{p_0}\right)^{\frac{R}{C_p}}\right] \quad (7)$$

In the neutral dry atmosphere, the temperature lapse rate is $\Gamma_{dry} = g/C_p$. Equation (7) is written as

$$z_{kap} = \frac{T_0}{\Gamma_{dry}}\left[1 - \left(\frac{\overline{p}}{p_0}\right)^{\frac{R\Gamma_{dry}}{g}}\right] \quad (8)$$

Another commonly-used coordinate is the log-pressure coor-dinate [23], which differs from the original height in the sense that the actual temperature differs from the mean surface temperature, as shown in Equation (9). This coordinate is also referred to as the isobaric coordinate system.

$$z_{log} = -\frac{RT_0}{g}\ln\left(\frac{\overline{p}}{p}\right) = -\frac{T_0}{\Gamma}\ln\left(\frac{T_0 - \Gamma z}{T_0}\right) \quad (9)$$

These three types of coordinates are obtained from different assumptions. The DB and KRB coordinates obey the
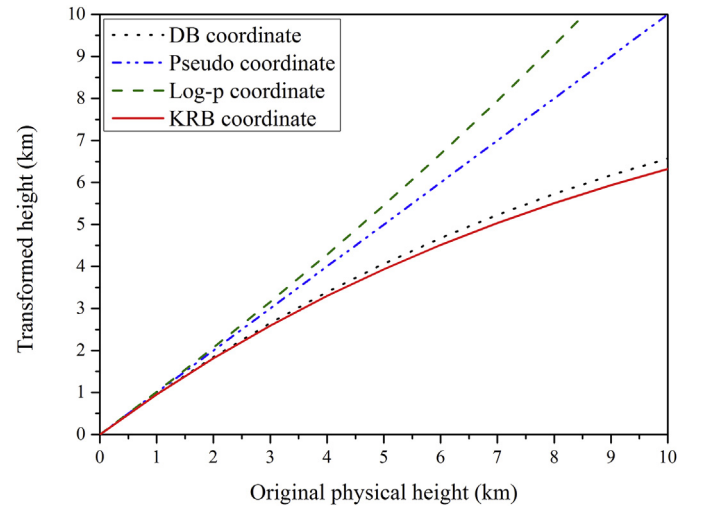
Fig. 2. Values of the transformation coefficient ξ under different temperature lapse rates.

Fig. 3. The relationship between the original physical height and several different transformed coordinates.

assumption$\partial h / \partial z = \partial z_{DB} / \partial z = \overline{\rho} / \rho_0$, while the pseudo height coordinate obeys the assumption$\partial z_{kap} / \partial z = \theta_0 / \overline{\theta}$. In the neutral dry atmosphere,$\theta_0 = \overline{\theta}$, so $z_{kap} = z$. In the log-pressure coordinate, $\partial z_{log} / \partial z = T_0 / \overline{T}$. The different assumptions reveal their different purposes and lead to different results. Fig. 3 summarizes the relationship between the original physical height and various transformed heights in the neutral dry atmosphere. In the log-pressure coordinate, the density no longer appears explicitly in the pressure gradient force [22]. The pseudo height and the original physical height are the same in this circumstance. In the DB and KRB coordinates, the density will also not appear if the anelastic assumption is adopted.

As mentioned above, the atmosphere layer is effectively compressed in the KRB coordinate, and the maximum height is 10 km, when the transformation coefficient ξ is taken as 10^{-4} m^{-1}, i.e. as $z \to \infty$, $h \to 10$ km. Equation (5) also shows that as the height $z \to 0$, the newly transformed height $h \to z$. This is shown in Fig. 4 for corresponding physical heights for a uniform vertical grid ($\Delta h = 1$ km) in the transformed vertical coordinate. The corresponding original heights of the three KRB height dash lines ($h = 9$ km, $h = 10$ km and the maximum height (about 8.4 km)) are not shown.

Meanwhile, in the KRB coordinate (shown as subscript 'h'), Kristóf et al. [26] introduced some transformed variables including pressure, density and temperature.

$$(p')_h = \left(\frac{\rho_0}{\overline{\rho}} p' \right)_z \tag{10}$$

$$(T)_h = (T - \overline{T} + T_0)_z = (T + \Gamma z)_z \tag{11}$$

$$(\rho)_h = (\rho - \overline{\rho} + \rho_0)_z \tag{12}$$

2.3. Summary of the new transformed equations in the KRB coordinate

A set of governing equations in KRB coordinate can be derived (Appendix A) and summarized as follows in Equations (13)–(21).

$$\frac{\partial u}{\partial x} + \frac{\partial v}{\partial y} + \frac{\partial w_h}{\partial h} = 0 \tag{13}$$

$$\frac{d(\rho_0 u)}{dt} = -\nabla p'_h + \rho_0 (\mu + \mu_t) \nabla^2 u + S_x \tag{14}$$

$$\frac{d(\rho_0 v)}{dt} = -\nabla p'_h + \rho_0 (\mu + \mu_t) \nabla^2 v + S_y \tag{15}$$

$$\frac{d(\rho_0 w_h)}{dt} = -\frac{\partial p'_h}{\partial h} + \rho_0 \beta (T_h - T_0) g + (\mu + \mu_t) \nabla^2 w_h + S_h \tag{16}$$

$$\frac{d \left(\rho_0 C_p T_h - p'_h \right)}{dt} = \nabla \cdot \left(k_{eff} \nabla T_h \right) \tag{17}$$

$$S_x = 2\Omega \left(\frac{w_h \cos \varphi}{1 - \xi h} - v \sin \varphi \right) \tag{18}$$

$$S_y = 2\rho_0 \Omega u \sin \varphi \tag{19}$$

$$S_h = \frac{\rho_0 \beta g \left(2\xi h - \xi^2 h^2 \right) (T_h - T_0)}{(1 - \xi h)^2} + \frac{2\rho_0 \Omega u \cos \varphi + \xi \rho_0 w_h^2}{1 - \xi h}$$
$$+ (\mu + \mu_t) \left(\xi^2 w_h - \xi (1 - \xi h) \frac{\partial w_h}{\partial h} \right) \tag{20}$$

$$S_T = \rho_0 Q_{ex} + J C_p \rho_0 w_n \left(\Gamma_s - \frac{g}{C_p} \right) \tag{21}$$
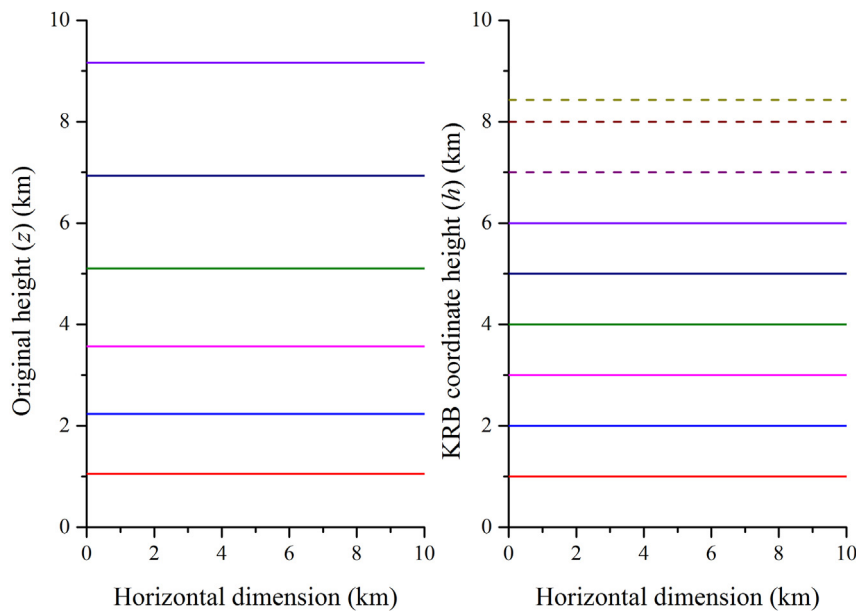

Fig. 4. A sketch of the difference between the physical vertical coordinate z and the new KRB coordinate h.

The last term in Equation (20) is a new term that does not exist in the model of Kristóf et al [26]. Its omission was probably due to the assumption in Kristóf et al [26] that turbulence takes place only at low altitudes in which the transformation makes little effect. We show in Appendix B using a scale analysis that the term should not be left out.

The KRB transformed equations are suitable for the pressure-based CFD solvers, such as the commercial CFD software Fluent. This is mainly due to the simpler continuity Equation (A15) in the transformed coordinate.

Three major questions remain. The first is whether the transformed mesoscale equations are accurate in predicting the microscale flow dynamics in a city. It is fairly easy to show that the transformed equations are equivalent to the original incompressible Navier–Stokes equations for a small height z (or transformed height h). The transformed equations are capable of representing both mesoscale and microscale flows in urban climate analyses.

The second question relates to turbulence modeling (parameterization). Consistent turbulence models should be used in both mesoscale and microscale flows. The types of two-equation models widely used in mesoscale and microscale climate modeling are the Mello-Yamada level 2.5 (MY) model [33] and the standard $k-\varepsilon$ model [29] respectively. The turbulence length scale is determined by the Monin-Obukhov (MO) length in the MY model, and by the turbulence kinetic energy k and its dissipation rate ε in the $k-\varepsilon$ model. Kim et al [25] found that the formation of the two models was similar, though the MY model neglected the pressure redistribution effect of buoyancy and shear. The associated wall function boundary conditions are different. The traditional wall function used in CFD does not consider atmospheric stability as does the MY model, which uses the MO length. For the preliminary study here, we have chosen the widely used standard $k-\varepsilon$ model as in Kristóf et al [26].

The third question involves the inability to resolve the hundreds of thousands of buildings in a city given the capacity of existing computers. We adopt the porous approach as suggested by Hang and Li [20,21]. Our proposed approach is simple. For the local region of concern, e.g. surrounding a particular building to be designed, the building geometry can be fully resolved, while for the remaining urban canopy layers, the porous turbulence model can be used. The porous model of Hang and Li [20,21] is based on the standard $k-\varepsilon$ model. The porous turbulence model can capture the major flow features as affected by buildings in the canopy layer. This is different from the typical canopy layer model in mesoscale urban climate modeling [8,28,42]. We refer to the combined porous and KRB approach as a city-scale CFD model (csCFD). In csCFD, we also add an absorbing layer [11] below the top boundary to avoid the effect of spurious waves.

3. Results

The implementation of city-scale CFD (csCFD) is based on commercial CFD software – Fluent (v6.3, ANSYS Inc, USA), which is widely-used in engineering applications with good parallel performance and great mesh generation, enabling user-friendly implementation. The Arakawa staggered C-Grid is widely used in mesoscale models such as WRF. Fluent software uses non-staggered unstructured grids which are ideal for complex geometry. We have chosen the third-order QUICK scheme for the convection terms and 2nd order center differencing for the diffusion terms. All simulations are performed in the transformed coordinate, but the results are converted back to the physical height for analysis.
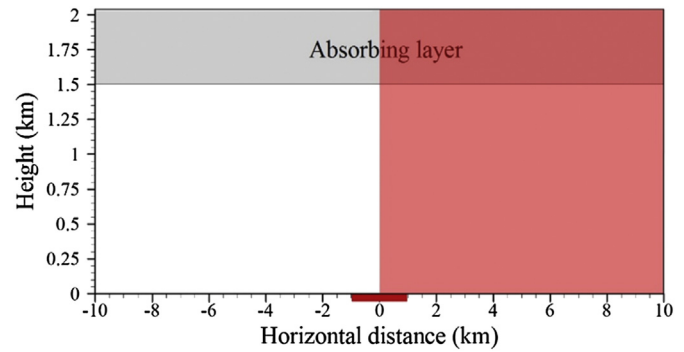

Fig. 5. The computational domain for simulating UHIC for a flat city.

Two case studies are shown here. The first is nighttime UHIC in a stable atmosphere with a constant lapse rate, comparing our prediction with the measured and simulated data in literature. The second is daytime UHIC as affected by heat flux, urban porosity and building heights.

3.1. Validation against LES prediction data for nighttime UHIC

Catalano et al [6] used the WRF-LES to simulate day and nighttime UHIC. A 3D ideal nighttime UHIC case is used here for validation. The city is infinitely long in the y-direction, so we only consider a 2D case. The computational domain is 20 km in the x-direction, and 2 km in the z-direction, as shown in Fig. 5. The width of the urban area is 2 km long and treated as a homogeneous flat surface (*flat city*). The urban area is highlighted in red in Fig. 5, (in the web version) and the surrounding area is rural. The grid spacing in x direction is 100 m and the first y grid is 0.1 m, with an increase ratio of 1.05. A similar grid independence test was carried out in Appendix C.

Only half of the domain was simulated, as the symmetry boundary is used for the middle axis. The pressure outlet boundary was adapted for the lateral boundary. To avoid the effect of spurious waves, an absorbing layer was added from a height of 2 km to the top of the boundary layer. The heat flux released from the urban area is 37 W m^{-2}, with no heat released from the rural area, which is as the same as Catalano's [6] simulation. The simulation was initialized with an ideal potential temperature profile with a constant potential temperature lapse rate $\Gamma = 0.005$ K m^{-1}. The thermal expansion coefficient is 0.0033 K^{-1}. The results at the simulation time of 6 h are shown by Catalano et al [6]. The initial velocity was zero and the initial temperature was 300 K. The initial TKE and its dissipation rate were set to 10^{-6} m^2 s^{-2} and 10^{-9} m^2 s^{-3}, respectively. The time step was set to 1 s, the simulated result from 5.5 to 6.5 h was averaged for analysis.

Three typical non-dimensional similarity parameters are defined below to describe the viscous, incompressible and stratified fluid. They are the Reynolds number (Re), the Froude number (Fr) and the Prandtl number (Pr). The Brunt–Väisälä frequency (N), sometimes referred to as the buoyancy frequency, is also important in the buoyancy driven flow.

$$N = (g\beta\partial T_a/\partial z)^{1/2} \tag{28}$$

$$Re = U_D D/\nu \tag{29}$$

$$Fr = U_D/ND \tag{30}$$

$$Pr = \nu/\kappa \tag{31}$$

where D is the length of the heat source, i.e. the urban area, which is used for length scale instead of the mixing height z_i, due to its independence in the experiment [32]. U_D is the convective velocity scale and is determined by the heat flux and the length scale

$$U_D = \left(g\beta DH_0/\rho_0 C_p\right)^{1/3} \tag{32}$$

The vertical velocity scale W_D is

$$W_D = U_D^2 \big/ ND \tag{33}$$

These scaled variables and non-dimensional similarity parameters allow the data from different experiments and simulations to be compared. Catalano et al [6] also used scaled variables to compare the results with other simulations and some laboratory experiments. Fig. 6 compares the scaled temperature and velocity between our study and other nighttime UHIC results, including both large eddy simulations and water tank experiments. Fig. 6a compares the scaled mean temperature profiles along the heat center from many results. The points represent the experimental data and the lines the simulation data, showing that the simulation result from csCFD generally agrees well with the other results. Due to the comparable coordinate and method, the simulation results from both this study and the study of Kristóf (water tank experiment simulation) are very similar compared to other results. Fig. 6b shows the scaled horizontal velocities. There is good agreement with the existing simulation model, but not with the water tank model. This may be due to the roughness height used in the wall function in the simulation, which might increase resistance in the simulation, so further improvement will be needed. We also noticed that the scale horizontal velocity near the ground in this study and in Yoshikado [49] is a little larger than others, which may

be due to the 2D and 3D simulation difference. The study here and Yoshikado are both 2D cases. Fuliotto et al. [15] also showed that while the 2D and 3D results can exhibit some differences, in general, 2D case can capture most of the major characteristics. Due to computational time limitations, we used the 2D case here, and the 3D case will be studied in the future. Fig. 6c shows the scaled vertical velocities, and the results are good compared with other data.

3.2. The impact of urban porosity, heat flux and urban height on UHIC

As a test case, we applied our model in Fluent to study UHIC as affected by heat flux and some morphology parameters such as building density (shown as porosity in the porous model) and average height of the buildings. Compared to some existing mesoscale models such as WRF, an advantage of the porous approach is its ability to consider the inhomogeneous porous media so that the height variation and different building densities can be fully considered [21].

We will consider a *flat city* as in Section 3.1 (Fig. 5), and also a *porous city,* treating the whole UCL area as porous media (Fig. 7a1). The city is 10 km ($D = 10$ km) in the x-direction and is infinite in the y-direction.

The porosity ϕ is defined as the fluid volume contained in the averaging volume divided by the total volume of the averaging volume [20]. For the cuboid-shaped buildings with the same height, the porosity is equal to the building density (referred to as plan area index) λ_p.

In this ideal city, the buildings are cubes of uniform size, the sides H of the cubes are 50 m. The width of the street is also H. Thus, the porosity is 0.75 and the morphology parameters building density λ_p and the frontal area density λ_f are both 0.25. This can be considered a low density city as defined in Grimmond and Oke [18]; i.e. low-density city ($\lambda_p \in [0.05\ 0.4]$), medium density city ($\lambda_p \in [0.3\ 0.5]$), high density city ($\lambda_p \in [0.5\ 0.8]$) and the high-rise city ($\lambda_p \in [0.4\ 1]$) based on data for typical cities. Wong et al
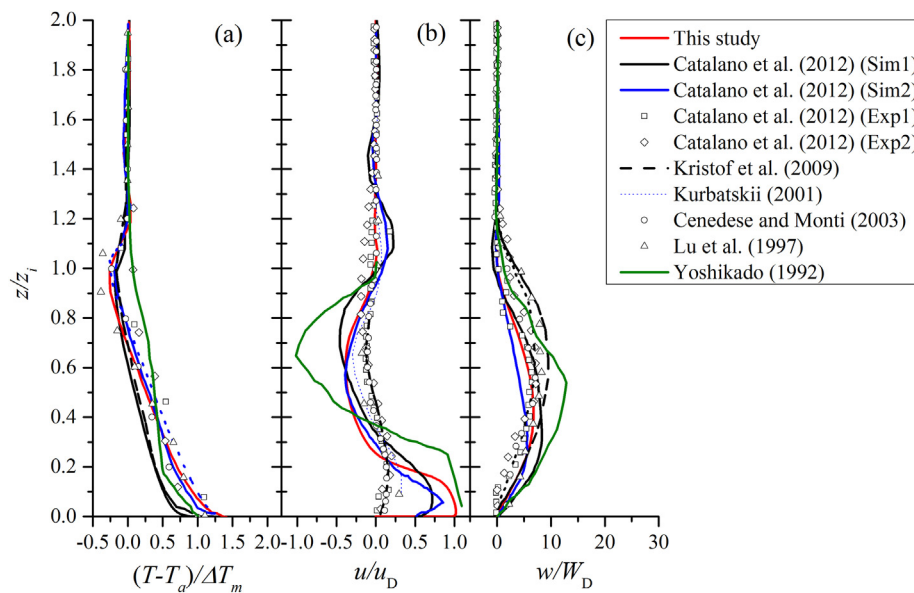

Fig. 6. Comparison of predicted scaled (a) vertical temperature profile, (b) horizontal wind speed at the city edge and (c) the vertical wind speed at the city center with data in the literature.
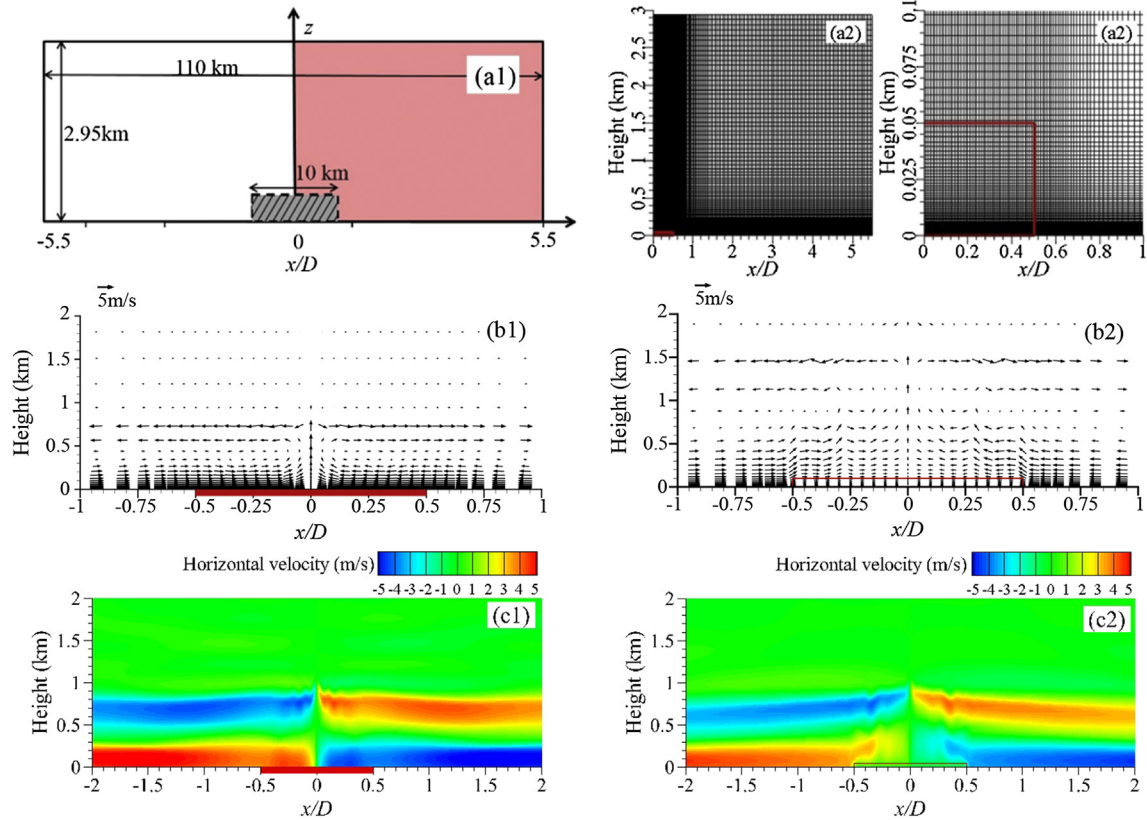
Fig. 7. (a1) The sketch of the computational area in the physical domain; (a2) A drawing of the mesh of the computational area. (b1) and (b2) are the vectors for porosity of 1 and 0.75; (c1) and (c2) are contour maps of the horizontal velocity for porosity of 1 and 0.75.

[45] also observed $\lambda_f = 0.25$ in the Kowloon area of Hong Kong. Meanwhile, the porous media are homogenous.

The initial condition is assumed to be stable, where the potential temperature lapse rate is 0.007 K m^{-1}. The height of the domain is set at 2.95 km. The length between the two lateral boundaries is 10 times of the length of the city area, and the computational domain is 110 km long. For the baseline case, the height of the porous city region is 50 m.

The basic boundary conditions are set as in Section 3.1. The urban heat is represented by sensible heat flux. But different from Section 3.1, the sensible heat flux in the rural area is 50 W m^{-2}, while the sensible heat flux in the city is 200 W m^{-2} for the baseline case. Due to the existence of porous media, only 75% of the sensible heat flux ($\phi = 0.75$) is released from the underlying surface in city, while the remaining 25% is released uniformly in the urban canopy layer.

Note that for the flat city case ($\phi = 1$), the city is treated as a homogenous plate which releases the same total sensible heat flux of 200 W m^{-2} as in the porous city case, but the influence of the building roughness is not considered. In both the flat city and the porous city, the roughness height in the rural area is ignored. The choice of heat flux is based on other studies of surface heat flux. Yang et al [50] calculated the ground surface heat flux for a simple courtyard, and showed that the maximum heat flux in the daytime can reach 300 W m^{-2}. For urban heat island circulation simulation studies, the heat flux in the city is usually around 100–200 W m^{-2} [52].

To obtain both the small scale characteristics in the city and the large scale phenomenon over the whole domain, the mesh must be fine in the city region, and coarse for the area outside the city for computational efficiency. In the vertical direction, the grid near the surface is finer so the heat transfer process near the surface is simulated correctly and the physics at the pedestrian level can be captured. The first mesh is 0.1 m above the underlying surface to fulfill the requirement of y^* [9]. The grid size in the vertical direction increases with a ratio of 1.05 until the grid is 50 m, and the grid remains 50 m from there to the top of the domain. The x-grid in and near the city region ($-0.6 \le x/D \le 0.6$) is set to 100 m to obtain detailed characteristics compared to the mesoscale model, and it is uniform. The x-grid far away from the city area ($x/D > 1.4$) is not as crucial, so the x-grid there is set to 500 m. Between these two regions, the x-grid increases from the city area to the direction outside the city with a ratio of 1.05, until the grid reaches 500 m. A plot of the chosen mesh of the computational area is shown in Fig. 7a2. The grid dependence was checked using three grid sizes, and the results were nearly identical.

The air flows were quasi-stationary after 10 h, and the average of two hours data from 10 h was considered as the quasi-steady state. Fig. 7b1 and b2 show the velocity vector between $-2 \le x/D \le 2$, where D is 10 km for the flat city and the porous city. The area in the rectangle represents the city region.

The results show that in both cases, the air flows in and converges above the center of the city area, and diverges at the mixing height. Due to the strong inversion layer in the initial and background temperature profile, the convergence area in the lower urban boundary layer (UBL) is thicker than the divergence area in the upper UBL. However, the velocity near the urban canopy layer was different for the two cases. In the flat city case, the horizontal velocity only decreased slightly near the center of the heated area above the surface. This is understandable, as the urban roughness

was not considered. Meanwhile, for the porous city case, as the effect of the building clusters is introduced by our porous turbulence model, only parts of the air penetrate into the city and others are lifted up above the city. The horizontal velocity in the city decreased significantly due to the porous media or the building clusters. This agrees with the prediction data of Hang and Li [20]. At the same time, the geometry of the plume also changed. For the flat city, only one plume is formed and the air is lifted up near the center of the heated plate by the plume. But in the porous city case, the air is lifted up along the area just above UCL.

Fig. 7c1 and c2 shows the contour maps of the horizontal velocity in the flat city and the porous city. In the porous city, the velocity decreased dramatically from about 4 m s^{-1} to 1 m s^{-1} in the urban canopy layer due to the blockage effect of the buildings, as demonstrated by the porous turbulence model.

Fig. 7c1 also shows that strong convergence occurred immediately above the center of the heat plate in the flat city case, and the convergence height is above the canopy layer in the porous city case. The strength of the convergence decreased due to the smaller pressure in the city region in the porous city case. In the upper part of the UBL, the influence of building clusters also changed the angle of the outward flow. In the clear case, the angle is steeper. We are aware of the fact that the angle is related to the magnitude of the heat flux. Although the total heat in the two city models is the same, our model can capture the physics when some heat is trapped in the canopy layer in the porous city case. This phenomenon is clear in Fig. 8a2 and b2. It shows the spatial distribution of the vertical velocity. The value of the maximum and minimum vertical

velocity was larger in the flat city than in the porous city case. In the flat city case, the air only rose up above the center portion of the heated area, but the air is lifted up in several areas above the city in the porous city case, even though the porous media and the underlying surface are both homogenous. Our predicted urban heat island circulation pattern also shows good agreement with other large eddy simulation results [43,52].

It is interesting to find some waves above the city area ($|x/D| \leq 0.5$) especially in the upper UBL, but the same waves do not exist in the mesoscale simulation of the UHIC when the grid space is large [17]. These waves are seen when the grid is finer probably because a fine grid size can capture a more detailed turbulence structure, although the proper turbulence structure will be shown in 3D simulation. The smooth contour maps have been widely reported in mesoscale UHIC simulations [17], and the wavelike variations have been frequently reported in UHIC simulated by LES [38].

Fig. 8c1 and c2 are the contour maps of the potential temperature for the two cases. In both cases, the maximum potential temperature appears near the center of the underlying surface of the city. The phenomenon of plume spread in the porous city case is clearly shown, in which the plume was formed above the top of UCL and the neck of the plume is also wider. Zooming in on the potential temperature near the edge of the city area in the porous city, the temperature increased quickly there, and is higher than the surrounding area. But such a phenomenon cannot be observed in the flat city. The abnormal high potential temperature is attributed to the positive vertical velocity in the corresponding area. But the
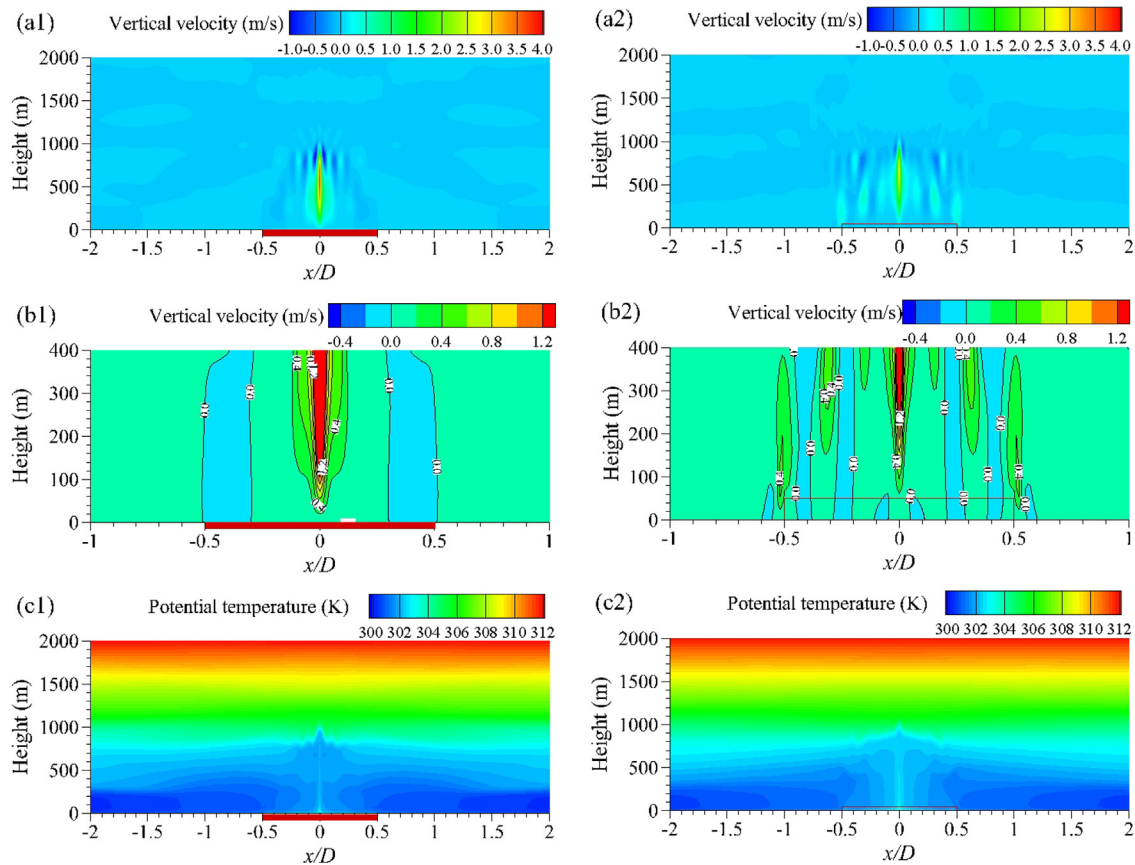

Fig. 8. (a1) and (a2) contour maps of the vertical velocity for porosity of 1 and 0.75; (b1) and (b2) a magnified urban region; (c1) and (c2) contour maps of the potential temperature at the quasi-steady state.
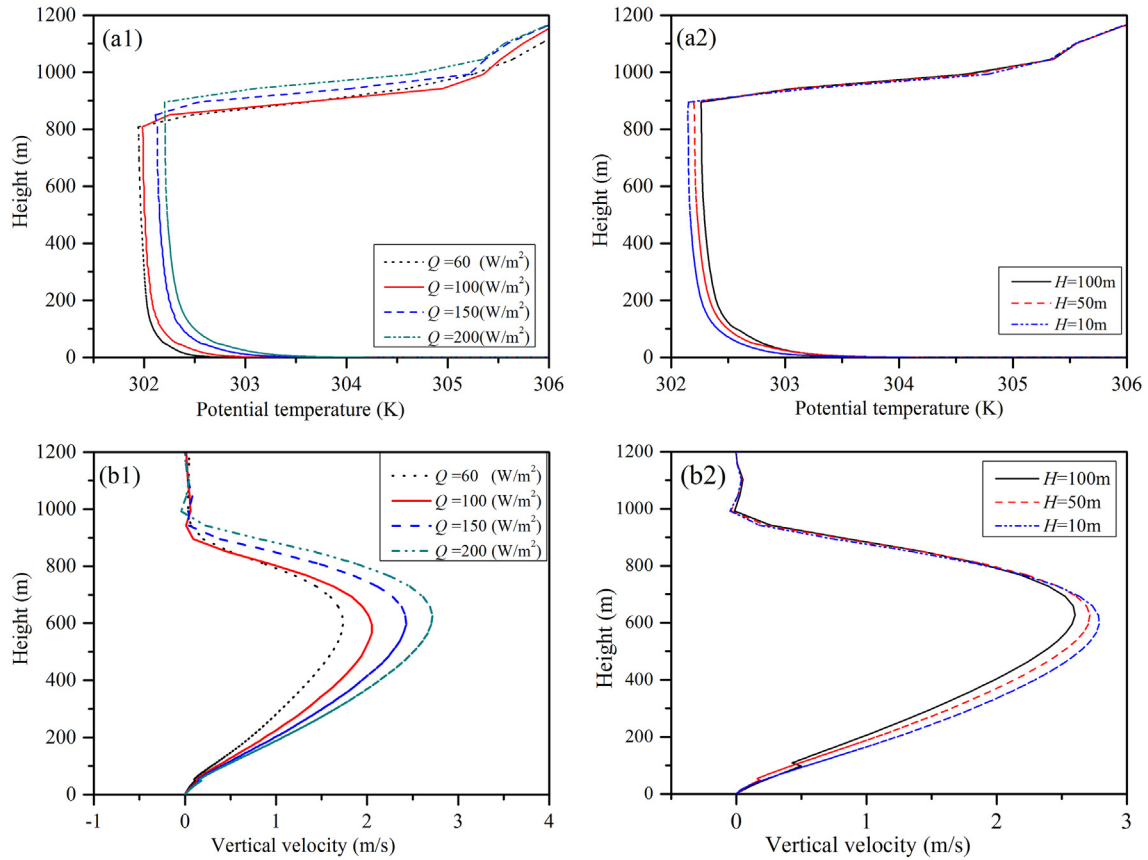
Fig. 9. (a1) The profiles of the potential temperature at x/D = 0 with different heat fluxes when the porosity is 0.75. (a2) Potential temperature profiles at the city center in these different cases. H is the height of the UCL. The profiles of the vertical velocity when the porosity is 0.75 at x/D = 0 with (b1) different heat fluxes and (b2) different urban canopy heights.

vertical velocity in the corresponding area in the flat city case is still zero.

The contribution to UHIC by sensible heat flux is studied by simulating UHIC under four different sensible heat fluxes in city, i.e. 60, 100, 150 and 200 W m^{-2} in the city region, while the heat flux of 50 W m^{-2} for the rural area is kept constant. Fig. 9a1 shows the profiles of the potential temperature at the city center ($x/D = 0$) for the porous city when the porosity is 0.75 at the quasi-steady state in different cases. As expected, the mixing height and the potential temperature of the center of the plume increased when the sensible heat flux increased. The large temperature gradient generates a large pressure gradient, and finally leads to a high value in the maximum horizontal and vertical velocity. Fig. 9b1 shows the profiles of the vertical velocity at the city center ($x/D = 0$). When the sensible heat flux increased, both the value of the maximum velocity and the height where the maximum velocity appears increased. The horizontal velocity at $|x/D| = 1$ and above the city area increased when the sensible heat flux increased. The angle of the outward flow increased when the sensible heat flux increased (the contour maps of the horizontal velocity are not shown here).

It is well known that the height of the urban canopy layer will change the shear stress in the canopy model and the porous model. This may also change the mesoscale UHIC. To study this, we set the previous case as the control case ($H = 50$ m), and changed the UHL height to 10 m ($H = 10$ m) and 100 m ($H = 100$ m) for comparison.

Note that the heat fluxes are identical for the three heights. The potential temperature and vertical velocity profiles at $x/D = 0$ in these cases at quasi-steady state is shown in Fig. 9a2, b2 and c2. The result shows that the mixing height did not change when the total heat was kept constant. The porosity and the total heat had already been set to the same value, so the difference was only contributed by the height of the UCL. The contribution of the height is very small. When the height of the UCL decreased to around 50 m the potential temperature in the plume decreased by 0.1 K. Even if the total heat in the volume was the same, when the UCL is higher, the potential temperature in the center line of the plume is higher. The reason for this is explained below.

Fig. 10a1, b1 and c1 shows the contour map of the horizontal velocity near the city area at quasi-steady state when the height of the UCL is changing and when the porosity is 0.75. When the UCL rose, the block effect of the city was more apparent, leading to a weaker convergence near the city. Meanwhile, the horizontal velocity in the UCL near the edge increased when the height increased. Fig. 10a2, b2 and c2 shows the contour map of the potential temperature near the city area at quasi-steady state as the height of the UCL is changing. A hole formed around $|x/D| = 0.4$ at the top of the city. Such a hole is an averaged expression of the entrainment in the unsteady process. When the height increased, the entrainment also increased. Since the velocity in the UCL is smaller when the UCL is higher, more heat will be trapped in the UCL. Therefore, the potential temperature in the plume center
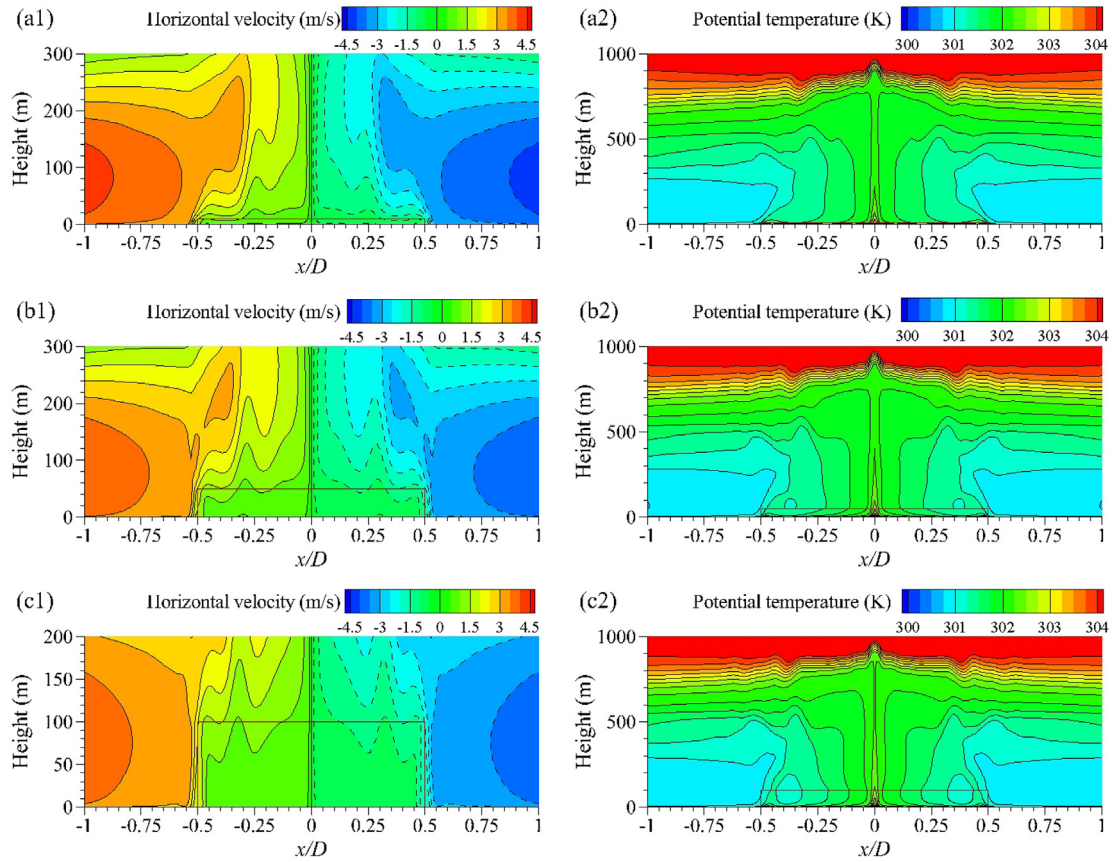
Fig. 10. The contour map of the horizontal velocity near the city area (a1, b1, c1) of UCL of 10, 50 and 100 m, The contour map of the potential temperature near the city area. (a2, b2, c2).

slightly increases.

4. Discussion

4.1. General discussion

Kristóf et al [26] already validated their KBR model for Coriolis force, compressibility and stratification effects. The KBR transformed equations for the mesoscale flows can adequately represent the atmospheric compressibility, while automatically converting to incompressible flows close to the surface. In this paper, we have successfully simulated the UHIC problem using a slightly revised version of this model. Our work has demonstrated the effectiveness of the KBR transformation, which has enabled application of a pressure based CFD solver to a meso-microscale flow problem.

Most existing mesoscale and microscale models are developed by meteorologists and wind engineers respectively, and they are only applicable to either mesoscale or microscale physics. It is pragmatic to use mesoscale models or microscale models on their own, as both the mesoscale and the microscale phenomenon co-exist in urban climate flows. We have demonstrated here that the KBR model can extend an existing pressure-based CFD solver to a city scale UHIC problem.

The UHIC phenomenon is important as it occurs when the synoptic wind is zero, when pollution and air quality are worst. To our knowledge, this is a very difficult problem for CFD to simulate.

Our evaluation was carried out by comparing data obtained from water tank experiments and other existing numerical models, and good agreement was shown.

4.2. Limitations

There are a number of major limitations in this paper. A RANS model was tested. The RANS models are widely known to be unable to predict accurate results for various types of flow phenomena around buildings, and it is also known that LES can provide much better results. This will be tested in the near future. Some other physical processes such as water vapor transport, cloud formation and precipitations were not considered in this model. This is also a weakness of all major CFD models, and capability extension is needed in future, as there is no fundamental difficulty in considering such microphysical phenomena. However, the existing CFD models also offer many capabilities that traditional mesoscale models cannot offer, e.g. consideration of complex building geometry, and simulation of both short and long wave radiation transport between multiple surfaces.

It is impossible to fully resolve all the buildings in a very large city in a computer simulation of wind flows due to the computational capacity constraints. Our porous turbulence model approach appears to capture the flow physics well. The ability of our model to treat most parts of the canopy layer as porous media, and the concerned region with full spatial resolution will be demonstrated

in a separate paper.

The development of UHIC usually comes with the evolution of the convective planetary boundary layer (PBL). In addition to a constant sensible heat flux to present the thermal differences between the city and the rural area, we need to prescribe hourly sensible heat flux profiles. This would allow us to analyze UHIC under more realistic conditions. We have already developed such a simple surface heat flux model for use with CFD, which will be presented in a future paper.

Meanwhile, solid validation is still needed for our model using field data. The evaluation is still preliminary here, as there is a lack of suitable field measurement data for UHIC, to the best of our knowledge. The small-scale field city model of Inagaki and Kanda [23] may be able to provide such data.

When the city was treated as porous media, we only considered the homogenous media, which is the simplest situation. To consider a more realistic city, the porous turbulence model should be improved, so the height and density variance can be considered using inhomogeneous porous media. In reality, the vertical flow resistance due to buildings is less than the horizontal. Therefore, such non-isotropic conditions should be considered.

Though Hang and Li [20] have evaluated the ability of the porous model in predicting wind-driven flows, the necessary modeling of the interaction of synoptic wind and the urban plumes, or the penetration of synoptic winds into a city is yet to be carried out. The CFD based meso-microscale model could in theory simulate a lot of phenomena, for example, the interaction between building plumes and UHIC, the interaction between the synoptic wind and the plume generated from urban heat island, the sea breeze wind in coastal cities, the slope wind when a city is located in a valley etc. After the moisture equation is added, it may also be used to predict the cumulus clouds above the city. All of these simulations should be evaluated in future.

5. Conclusions

Based on the KRB coordinate transformation proposed by Kristóf, Rácz and Balogh [26]; we successfully implemented the new model using a commercial CFD package for studying UHIC. The meso-microscale model was shown to be able to describe the mesoscale and microscale flow phenomena. We also revealed the silent features of the KRB coordinate transformation including the use of the constant transformation coefficient, the pressure-based coordinate, and the simpler continuity equation for the pressure-based solvers. An existing porous turbulence model was used for modeling the urban canopy later except in some local areas, where the microscale flows are of interest. Our predictions of urban heat island circulation agree well with existing data from the literature using large eddy simulation and mesoscale models, and laboratory experiments. We further demonstrated the ability of the new model for modeling urban heat island circulation for different city settings. The model correctly predicted that the sensible heat flux is the main factor influencing the strength of the UHIC and the mixing height. When the porous model was considered, the velocity in the urban canopy layer decreased. The height of the UCL slightly influences the potential temperature in the center and influences the strength of the entrainment of the urban plume. There are a number of other meso-microscale models such as A2C [47], it seems that the KRB model offers a sound complementary approach, with much potential for further development.

Appendix A. Derivation of the KRB transformed governing equations of the meso-microscale atmospheric flows

A1. The reference state

The reference state is the hydrostatic atmosphere. The temperature lapse rate Γ is constant. The temperature, pressure and the density of the reference state can be calculated by Equations (2) to (5) respectively [24].

$$\overline{T} = T_0 - \Gamma z \tag{A1}$$

$$\overline{p} = p_0(1 - \Gamma z/T_0)^{g/(R\Gamma)} \tag{A2}$$

$$\overline{\rho} = \rho_0\left(1 - \frac{\Gamma z}{T_0}\right)^{\frac{g}{R\Gamma} - 1} \tag{A3}$$

$$\Gamma \equiv -\frac{\partial \overline{T}}{\partial z} \tag{A4}$$

where the subscript '0' represents the constant value at sea level. In the standard atmosphere [7], the pressure at sea level (p_0) is 1013.25 hPa, the temperature at sea level (T_0) is 288.15 K, and the gas constant for dry air (R) is 287.05 J kg^{-1} K^{-1}. g is gravity (9.8 m s^{-2}).

Based on hydrostatic Equation (6), the reference state density in the non-isothermal atmosphere can be calculated by the exponential Equation (7)

$$\frac{\partial \overline{p}}{\partial z} = -\overline{\rho} g \tag{A5}$$

$$\overline{\rho} = \frac{p_0}{R\overline{T}} e^{-\int_0^H \frac{g}{R(T_0 - \Gamma z)} \partial z} \tag{A6}$$

A2. The transformation

From Equation (5) in the main text, we have

$$\frac{\partial h}{\partial z} = e^{-\xi z} = 1 - \xi h \tag{A7}$$

The vertical velocity w is

$$w = \frac{\partial z}{\partial t} = \frac{\partial z}{\partial h}\frac{\partial h}{\partial t} = \frac{1}{1 - \xi h}\frac{\partial h}{\partial t} = e^{\xi z} w_h \tag{A8}$$

This is an interesting result, as the transformed vertical velocity decays upward in line with the air density (Equation (8) in the main text). The velocity vector in the KRB coordinate can be written as

$$\vec{V} = \left[u\,\vec{i}, v\,\vec{j}, w\,\vec{k}\right] = \left[u\,\vec{i}, v\,\vec{j}, e^{\xi z} w_h\,\vec{k}\right] \tag{A9}$$

The gradient-related terms are

$$\nabla = \frac{\partial}{\partial x} + \frac{\partial}{\partial y} + \frac{\partial}{\partial z} = \frac{\partial}{\partial x} + \frac{\partial}{\partial y} + \frac{\partial}{\partial h}\frac{\partial h}{\partial z} = \frac{\partial}{\partial x} + \frac{\partial}{\partial y} + e^{-\xi z}\frac{\partial}{\partial h} \quad (A10)$$

$$\overrightarrow{V}\nabla = u\frac{\partial}{\partial x} + v\frac{\partial}{\partial y} + w\frac{\partial}{\partial z} = u\frac{\partial}{\partial x} + v\frac{\partial}{\partial y} + w_h\frac{\partial}{\partial h} \quad (A11)$$

$$\nabla\overrightarrow{V} = \frac{\partial u}{\partial x} + \frac{\partial v}{\partial y} + \frac{\partial w}{\partial z} = \frac{\partial u}{\partial x} + \frac{\partial v}{\partial y} + \frac{\partial w_h}{\partial h} - \xi e^{-\xi z}w_h \quad (A12)$$

Therefore, for the variables other than vertical velocity w, which is represented as ψ:

$$\frac{d\psi}{dt} = \frac{\partial\psi}{\partial t} + u\frac{\partial\psi}{\partial x} + v\frac{\partial\psi}{\partial y} + w\frac{\partial\psi}{\partial z} = \frac{\partial\psi}{\partial t} + u\frac{\partial\psi}{\partial x} + v\frac{\partial\psi}{\partial y} + w_h\frac{\partial\psi}{\partial h}$$

$$(A13)$$

For the vertical velocity:

$$\frac{dw}{dt} = \frac{\partial w}{\partial t} + u\frac{\partial w}{\partial x} + v\frac{\partial w}{\partial y} + w\frac{\partial w}{\partial z}$$
$$= e^{\xi z}\left(\frac{\partial w_h}{\partial t} + u\frac{\partial w_h}{\partial x} + v\frac{\partial w_h}{\partial y} + w_h\frac{\partial w_h}{\partial h}\right) + e^{2\xi z}w_h^2\zeta \quad (A14)$$

The Laplacian ∇^2 related terms are:

$$\nabla^2 u = \frac{\partial^2 u}{\partial x^2} + \frac{\partial^2 u}{\partial y^2} + \frac{\partial^2 u}{\partial z^2} = \frac{\partial^2 u}{\partial x^2} + \frac{\partial^2 u}{\partial y^2} + e^{-2\xi z}\frac{\partial^2 u}{\partial h^2} - e^{-\xi z}\xi\frac{\partial u}{\partial h}$$

$$(A15)$$

$$\nabla^2 v = \frac{\partial^2 v}{\partial x^2} + \frac{\partial^2 v}{\partial y^2} + \frac{\partial^2 v}{\partial z^2} = \frac{\partial^2 v}{\partial x^2} + \frac{\partial^2 v}{\partial y^2} + e^{-2\xi z}\frac{\partial^2 v}{\partial h^2} - \xi e^{-\xi z}\frac{\partial v}{\partial h} \quad (A16)$$

$$\nabla^2 w = e^{\xi z}\frac{\partial^2 w_h}{\partial x^2} + e^{\xi z}\frac{\partial^2 w_h}{\partial y^2} + e^{-\xi z}\frac{\partial^2 w_h}{\partial h^2} + \xi\frac{\partial w_h}{\partial h} + e^{\xi z}\xi^2 w_h$$

$$(A17)$$

A3. The continuity equation

The purpose of any coordination transformation is either to write the physical law in a simpler form, or modify it to suit a particular solution method. The anelastic continuity equation for the mesoscale atmosphere is Equation (A18).

$$\overline{\rho}\nabla\overrightarrow{V} + w\frac{\partial\overline{\rho}}{\partial z} = 0 \quad (A18)$$

Substitute Equations (2), (A7), (A8) and (A12) into (A18), the continuity equation with the anelastic assumption in the KRB coordinate becomes:

$$\frac{\partial u}{\partial x} + \frac{\partial v}{\partial y} + \frac{\partial w_h}{\partial h} = 0 \quad (A19)$$

Fortunately Equation (A19) maintains the same format as the continuity equation for the general incompressible flows, although it actually governs a compressible flow problem. The transformed Equation (A19) in the KRB coordinate enables the use of the pressure-based CFD model. The idea is similar to the traditional log-pressure coordinate. It is known that the continuity equation in the pressure or log-pressure coordinate is simpler than its corresponding version in the original z coordinate.

A4. The momentum equation

In the mesoscale atmosphere, the momentum equation can be written as Equation (A20):

$$\frac{d\overrightarrow{V}}{dt} = -\frac{1}{\rho}\nabla p + \overrightarrow{g} + \overrightarrow{F}_c + \overrightarrow{F}_f + \overrightarrow{F}_t \quad (A20)$$

where the last three terms represent the Coriolis effect $\overrightarrow{F}_c$, the friction effect $\overrightarrow{F}_f$ and the turbulence effect $\overrightarrow{F}_t$, respectively. Although the friction effect is often omitted in the mesoscale atmosphere, it has a significant influence on near surface flows. Therefore it should not be ignored in our meso-micro scale model, which focuses on the interaction between the mesoscale and the microscale environment.

The Coriolis' effect term is calculated by Equation (A21), which changes a little in the KRB coordinate, as shown in Equation (A22):

$$\overrightarrow{F}_c = 2\overrightarrow{\Omega} \times \overrightarrow{V}$$
$$= \overrightarrow{i}\,2\Omega(w\cos\varphi - v\sin\varphi) + \overrightarrow{j}\,2\Omega u\sin\varphi - \overrightarrow{k}\,2\Omega u\cos\varphi$$

$$(A21)$$

$$\overrightarrow{F}_c = 2\overrightarrow{\Omega} \times \overrightarrow{V}$$
$$= \overrightarrow{i}\,2\Omega(w_h e^{\xi z}\cos\varphi - v\sin\varphi) + \overrightarrow{j}\,2\Omega u\sin\varphi$$
$$- \overrightarrow{k}_h\,2\Omega u\cos\varphi \quad (A22)$$

The turbulent term $\overrightarrow{F}_t$ is similar to the friction term $\overrightarrow{F}_f$. The only difference is the value of turbulent viscosity μ_t and molecular viscosity μ. Taking the friction term as an example, as friction occurs near the ground or buildings, where the density changes are very small, the ground level density is used here. In the Cartesian coordinate, the friction term is

$$\overrightarrow{F}_f = \nabla\overrightarrow{\tau} \cong \frac{\mu}{\rho_0}\nabla^2\overrightarrow{V} \quad (A23)$$

For the horizontal velocity, Equations (A24) and (A25) are the friction terms, multiplying ρ_0 in the KRB coordinate.

$$\rho_0\frac{\mu}{\rho_0}\nabla^2 u = \mu\left(\frac{\partial^2 u}{\partial x^2} + \frac{\partial^2 u}{\partial y^2} + e^{-2\xi z}\frac{\partial^2 u}{\partial h^2} - \xi e^{-\xi z}\frac{\partial u}{\partial h}\right) \quad (A24)$$

$$\rho_0\frac{\mu}{\rho_0}\nabla^2 v = \mu\left(\frac{\partial^2 v}{\partial x^2} + \frac{\partial^2 v}{\partial y^2} + e^{-2\xi z}\frac{\partial^2 v}{\partial h^2} - \xi e^{-\xi z}\frac{\partial v}{\partial h}\right) \quad (A25)$$

For the vertical velocity, Equation (A26) is the friction term multiplying $\overline{\rho}$ in the KRB coordinate.

$$\overline{\rho}\frac{\mu}{\rho_0}\nabla^2 w = \mu\left(\frac{\partial^2 w_h}{\partial x^2} + \frac{\partial^2 w_h}{\partial y^2} + e^{-2\xi z}\frac{\partial^2 w_h}{\partial h^2} - \xi e^{-\xi z}\frac{\partial w_h}{\partial h}\right) + \mu\xi^2 w_h$$

$$(A26)$$

The friction term contributes most near the ground, and a little at high altitude. As $z \to 0$, $e^{-2\xi z} \to 1$. At high altitude, $e^{-2\xi z}$ changes but $\partial^2 u/\partial h^2$, $\partial^2 v/\partial h^2$ and $\partial^2 w_h/\partial h^2$ are small. Therefore, the coefficient $e^{-2\xi z}$ of the third terms in (A24), (A25) and (A26) is replaced by 1. Thus the third term in the right hand side of Equation (A26) can be ignored. However, a simple dimensionless analysis reveals that the last two terms in Equation (A26) cannot be ignored.

Following the above, the horizontal velocity equation is obtained below.

$$\frac{du}{dt} = -\frac{1}{\rho_0}\nabla p'_h + 2\Omega\left(w_h e^{\xi z}\cos\varphi - v\sin\varphi\right) + (\mu + \mu_t)\nabla^2 u \tag{A27}$$

$$\frac{dv}{dt} = -\frac{1}{\rho_0}\nabla p'_h + 2\Omega u\sin\varphi + (\mu + \mu_t)\nabla^2\vec{V} \tag{A28}$$

In a pressure-based CFD model, the governing equations are often written in the conservative form. Rearrange Equations (A27) and (A28)

$$\frac{d(\rho_0 u)}{dt} = -\nabla p'_h + \rho_0 2\Omega\left(w_h e^{\xi z}\cos\varphi - v\sin\varphi\right) + \rho_0(\mu + \mu_t)\nabla^2 u \tag{A29}$$

$$\frac{d(\rho_0 v)}{dt} = -\nabla p'_h + 2\rho_0\Omega u\sin\varphi + \rho_0(\mu + \mu_t)\nabla^2 v \tag{A30}$$

The vertical velocity equation is

$$\bar{\rho}\frac{dw}{dt} = -\frac{\partial p'}{\partial z} - \frac{\partial\bar{p}}{\partial z} - \rho g + \bar{\rho}2\Omega u\cos\varphi + \bar{\rho}(\mu + \mu_t)\nabla^2 w \tag{A31}$$

Applying Equation (A8), the left hand side of Equation (A31) is

$$\bar{\rho}\frac{dw}{dt} = \rho_0\left(\frac{dw_h}{dt}\right)_h + \rho_0 e^{\xi z}w_h^2\zeta \tag{A32}$$

The corrected pressure term, which is the first term on the right hand side of Equation (A31), is

$$-\frac{\partial p'}{\partial z} = -\frac{\partial}{\partial z}\left(\frac{\bar{\rho}}{\rho_0}p'_h\right) = \xi p'_h e^{-\xi z} - e^{-2\xi z}\frac{\partial p'_h}{\partial h}$$
$$= -\frac{\partial p'_h}{\partial h} + \xi p'_h e^{-\xi z} + \left(1 - e^{-2\xi z}\right)\frac{\partial p'_h}{\partial h} \tag{A33}$$

The second and third terms of the right hand side of Equation (A31) are the buoyancy terms. Substitute Equation (18) in the main text, the buoyancy term is

$$\bar{\rho}g - \rho g = -(\rho_h - \rho_0)g \tag{A34}$$

Apply the Boussinesq assumption, Equation (A34) becomes

$$\bar{\rho}g - \rho g = -(\rho_h - \rho_0)g = \rho_0\beta(T_h - T_0)g \tag{A35}$$

Substitute Equations (A16), (A25), (A32) and (A33) into Equation (A35), the vertical momentum equation in KRB coordinate is

$$\rho_0\left(\frac{dw_h}{dt}\right)_h + \rho_0 e^{\xi z}w_h^2\zeta = -\frac{\partial p'_h}{\partial h} + \xi p'_h e^{-\xi z} + \left(1 - e^{-2\xi z}\right)\frac{\partial p'_h}{\partial h}$$
$$+ \rho_0\beta(T_h - T_0)g + \bar{\rho}2\Omega u\cos\varphi$$
$$+ (\mu + \mu_t)\xi^2 w_h + (\mu + \mu_t)\xi^2 w_h \tag{A36}$$

Rearrange Equation (A37):

$$\rho_0\left(\frac{dw_h}{dt}\right)_h = -\frac{\partial p'_h}{\partial h} + \rho_0\beta(T_h - T_0)g + (\mu + \mu_t)\nabla^2 w_h + S_h \tag{A37}$$

where $S_h = \xi p'_h e^{-\xi z} + (1 - e^{-2\xi z})\partial\frac{p'_h}{\partial h + \rho_0 e^{-\xi z}2\Omega u\cos\varphi - \rho_0 e^{\xi z}w_h^2\zeta + (\mu + \mu_t)\xi^2 w_h}$

In the pressure-based CFD models, when the pressure gradient exists in the source term, the convergence can be difficult. To eliminate the pressure gradient in the source term, we follow

Kristóf et al's [26] assumption, using the pressure gradient of the reference state as the pressure gradient in the source term. In the reference state, the vertical velocity is zero, so Equation (A36) is simplified as

$$-\frac{\partial p'_h}{\partial h} + \xi p'e^{-\xi z} + \left(1 - e^{-2\xi z}\right)\frac{\partial p'_h}{\partial h} + \rho_0\beta(T_h - T_0)g + \bar{\rho}2\Omega u\cos\varphi$$
$$= 0 \tag{A38}$$

The pressure gradient in the reference state is

$$\frac{\partial p'_h}{\partial h} = e^{2\xi z}\left(\rho_0\beta(T_h - T_0)g + \bar{\rho}2\Omega u\cos\varphi + \xi p'e^{-\xi z}\right) \tag{A39}$$

Substitute Equation (A39) into source term,

$$S_h = \rho_0\beta g\left(e^{2\xi z} - 1\right)(T_h - T_0) + \rho_0 e^{\xi z}2\Omega u\cos\varphi + \xi e^{\xi z}\left(p'_h - \rho_0 w_h^2\right) + (\mu + \mu_t)\xi^2 w_h \tag{A40}$$

A5. The Energy Equation

Unlike in Kristóf et al [26], both the potential temperature equation in the mesoscale model and the temperature equation in the pressure-based CFD model are derived here directly from the first law of thermodynamics (Equation (A41)) [24]. The density is replaced by the reference density as per the previous assumption.

$$C_p\frac{dT}{dt} - \frac{1}{\rho}\frac{dp}{dt} = Q_{ex} \tag{A41}$$

where Q_{ex} is the external heat source.

Substitute Equation (1) in Equation (A41):

$$\bar{\rho}C_p\frac{d}{dt}\left(\bar{T} + T'\right) - \frac{d}{dt}\left(\bar{p} + p'\right) = \bar{\rho}Q_{ex} \tag{A42}$$

Substitute Equations (A1), (10) and (11) into (A42):

$$-\bar{\rho}e^{\xi z}C_p w_h\Gamma + \bar{\rho}C_p\frac{d}{dt}(T_h - T_0) + \bar{\rho}e^{\xi z}gw_h - \frac{d}{dt}\left(\frac{\rho_s}{\rho_0}p'_h\right) = \bar{\rho}Q_{ex} \tag{A43}$$

The last term of the left hand side of Equation (A43) is

$$\frac{d}{dt}\left(\frac{\rho_s}{\rho_0}p'_h\right) = e^{-\xi z}\frac{dp'_h}{dt} + \xi p'_h w_h \tag{A44}$$

So Equation (A43) is

$$\bar{\rho}C_p\frac{dT_h}{dt} = \bar{\rho}Q_{ex} + C_p\bar{\rho}e^{\xi z}w_h\left(\Gamma - \frac{g}{C_p}\right) + e^{-\xi z}\frac{dp'_h}{dt} + \xi p'_h w_h \tag{A45}$$

Multiply $\frac{\rho_0}{\bar{\rho}}$ in both sides of Equation (A45), we have:

$$\rho_0 C_p\frac{dT_h}{dt} - \frac{dp'_h}{dt} = \rho_0 Q_{ex} + C_p\rho_0 e^{\xi z}w_h\left(\Gamma - \frac{g}{C_p}\right) + e^{\xi z}\xi p'_h w_h \tag{A46}$$

The coordinate transformation of the internal force term S_f and the turbulent term S_t is similar, as in the momentum equation, and it is not repeated again. These terms in the KRB coordinate are

$$S_f + S_t = \nabla\cdot\left(k_{eff}\nabla T_h\right) \tag{A47}$$

where k_{eff} is the sum of molecular conductivity and turbulent thermal conductivity.

Rearrange Equation (A47) as the form used in Fluent:

$$\frac{d\left(\rho_0 C_P T_h - p'_h\right)}{dt} = \nabla \cdot \left(k_{\text{eff}} \nabla T_h\right) + S_T \tag{A48}$$

$$S_T = \rho_0 Q_{ex} + C_p \rho_0 e^{\xi z} w_h \left(\Gamma - \frac{g}{C_p}\right) + e^{\xi z} \xi p'_h w_h \tag{A49}$$

Note again that the magnitude of the transformation coefficient ξ is 10^{-4}. Compared to other terms, the last term in Equation (A49) is small enough to ignore. Therefore, the source term of the energy equation is

$$S_T = \rho_0 Q_{ex} + J C_p \rho_0 w_n \left(\Gamma - \frac{g}{C_p}\right) \tag{A50}$$

A6. Turbulence equations

The standard $k-\varepsilon$ turbulence model is used here as it is widely used and easy to implement. Similar to the energy model, the standard $k-\varepsilon$ model in the KRB coordinate is

$$\frac{d}{dt}(\rho_0 k) = \nabla \cdot \left(\left(\mu_s + \frac{\mu_t}{\sigma_k}\right) \nabla k\right) + G_k + G_{buo} - \rho_0 \varepsilon \tag{A51}$$

$$\frac{d}{dt}(\rho_0 \varepsilon) = \nabla \cdot \left(\left(\mu_s + \frac{\mu'_h}{\sigma_\varepsilon}\right) \nabla \varepsilon\right) + C_{1\varepsilon} \frac{\varepsilon}{k}(G_k + C_{3\varepsilon} G_b) - C_{2\varepsilon} \rho_0 \frac{\varepsilon^2}{k} \tag{A52}$$

where

$$G_k = \mu_t \left(\frac{\partial u_i}{\partial x_j} + \frac{\partial u_j}{\partial x_i}\right) \frac{\partial u_i}{\partial x_j} \tag{A53}$$

In the mesoscale atmosphere with buoyancy effect, the generation of turbulence kinetic energy due to buoyancy G_{buo} is changed to Equation (A54) to consider atmospheric stability. The stability is calculated through Equation (A28) by an approximate relationship between the temperature lapse rate and potential temperature lapse rate [54].

$$G_{buo} = -\beta g \frac{\mu_t}{Pr_t} \left(\frac{\partial T}{\partial z} + \frac{g}{C_p}\right) = -\beta g \frac{\mu_t}{Pr_t} \left(\frac{\partial T_h}{\partial h} - \Gamma + \frac{g}{C_p}\right) = G_b + S_k \tag{A54}$$

Equation (A51) is written as

$$\frac{d}{dt}(\rho_0 k) = \nabla \cdot \left(\left(\mu_s + \frac{\mu_t}{\sigma_k}\right) \nabla k\right) + G_k + G_b - \rho_0 \varepsilon + S_k \tag{A55}$$

$$G_b = -\beta g \frac{\mu_t}{Pr_t} \frac{\partial T_h}{\partial h} \tag{A56}$$

$$S_k = \beta g \frac{\mu_t}{Pr_t} \left(\Gamma - \frac{g}{C_p}\right) \tag{A57}$$

The transformed source of the turbulence dissipation rate is similar:

$$\frac{d}{dt}(\rho_0 \varepsilon) = \nabla \cdot \left(\left(\mu_s + \frac{\mu'_t}{\sigma_\varepsilon}\right) \nabla \varepsilon\right) + C_{1\varepsilon} \frac{\varepsilon}{k}(G_k + C_{3\varepsilon} G_b) - C_{2\varepsilon} \rho_0 \frac{\varepsilon^2}{k} + S_\varepsilon \tag{A58}$$

$$S_\varepsilon = C_{1\varepsilon} C_{3\varepsilon} \frac{\varepsilon}{k} \beta g \frac{\mu_t}{Pr_t} \left(\Gamma - \frac{g}{C_p}\right) \tag{A59}$$

Note in the KRB coordinate, all terms involving $e^{\xi z}$ need to be expressed as a function of h.

Appendix B. Scale analysis of the momentum equations

The scale analysis of the momentum equations is shown here. We define the following characteristic scales of the field variables based on observed values for the city environment as Table B1. For urban heat island analysis, the length of the city domain (D) replaces the length scale for the non-dimensional numbers, such as the Reynolds number etc.

Table B1
The scale number of the domain.

U	~	1	m s^{-1}	Horizontal velocity scale
W	~	10^{-2}	m s^{-1}	Vertical velocity scale
L	~	$10^4–10^5$	m	Length scale
D	~	10^4	m	City length scale
H	~	10^3	m	Depth scale
ξ	~	10^{-4}	m^{-1}	Transformation coefficient
Re	~	10^9		Reynolds number
N	~	10^{-2}		Buoyancy frequency
β	~	3×10^{-3}	K^{-1}	Thermal expansion coefficient

Table B2 shows the scale analysis of the horizontal momentum equation. The main contributor to the horizontal momentum equation is term B, the scale of pressure gradient is obtained by assuming the ideal gas law for the atmosphere. Terms C, D, E are related to the viscosity. When $\xi L^2/H << 1$, i.e. $L << 100\sqrt{H}$, the term F can be ignored. Recall that in UHIC analysis, the length scale L is replaced by the city scale D to improve the accuracy of the non-dimensional number. The fact that city diameter D can be 10 times the atmospheric depth H. So the last term F only can be ignored when the depth scale is less than 100 m. Therefore, for city scale UHIC analysis, the last term cannot be ignored. Whether term F can be ignored in other atmospheric phenomena depends on the particular conditions.

Table B2
The terms in horizontal momentum equation for scale analysis.

	A	B	C	D	E	F
x-equation	$\frac{du}{dt}$	$\frac{1}{\rho_0} \frac{\partial p'_h}{\partial x}$	$\frac{\mu_{\text{eff}}}{\rho_0} \frac{\partial^2 u}{\partial x^2}$	$\frac{\mu_{\text{eff}}}{\rho_0} \frac{\partial^2 u}{\partial y^2}$	$\frac{\mu_{\text{eff}}}{\rho_0} e^{-2\xi z} \frac{\partial^2 u}{\partial h^2}$	$\frac{\mu_{\text{eff}}}{\rho_0} \xi e^{-\xi z} \frac{\partial u}{\partial h}$
y-equation	$\frac{dv}{dt}$	$\frac{1}{\rho_0} \frac{\partial p'_h}{\partial y}$	$\frac{\mu_{\text{eff}}}{\rho_0} \frac{\partial^2 v}{\partial x^2}$	$\frac{\mu_{\text{eff}}}{\rho_0} \frac{\partial^2 v}{\partial y^2}$	$\frac{\mu_{\text{eff}}}{\rho_0} e^{-2\xi z} \frac{\partial^2 v}{\partial h^2}$	$\frac{\mu_{\text{eff}}}{\rho_0} \xi e^{-\xi z} \frac{\partial u}{\partial h}$
scales	$\frac{U^2}{L}$	$\frac{R\delta T}{L}$	$\frac{\mu_{\text{eff}}}{\rho_0} \frac{U}{L^2}$	$\frac{\mu_{\text{eff}}}{\rho_0} \frac{U}{L^2}$	$\frac{\mu_{\text{eff}}}{\rho_0} \frac{U}{H^2}$	$\frac{\mu_{\text{eff}}}{\rho_0} \xi \frac{U}{H}$
Using non-dimensional number	$\frac{U^2}{L}$	$\frac{RN^2 H}{g\beta L}$	$\frac{1}{\text{Re}} \frac{U^2}{L}$	$\frac{1}{\text{Re}} \frac{U^2}{L}$	$\frac{1}{\text{Re}} \frac{U^2 L}{H^2}$	$\xi \frac{1}{\text{Re}} \frac{U^2 L}{H}$
Divided by $\frac{U^2}{L}$	1	$\frac{RN^2 H}{g\beta U^2}$	$\frac{1}{\text{Re}}$	$\frac{1}{\text{Re}}$	$\frac{1}{\text{Re}} \frac{L^2}{H^2}$	$\xi \frac{1}{\text{Re}} \frac{L^2}{H}$

Similarly, Table B3 shows the scale analysis of the vertical momentum equation. Compare terms B and I, when $1/H << \xi$, which is true for UHIC, term I can be ignored. Compare terms C, K and L, we have $g/U >> \rho_0 H N^2 >> f_0$. Therefore, in UHIC, terms K and L can be ignored. Meanwhile, it is worth noting that when the vertical length scale increases to 10^4 or even higher, terms I, K, and L should not be ignored. Compare terms D to H, similar to term F in Table B2, term G cannot be ignored. Term H can be ignored only

when $D < < 10^4$. So term H can be ignored for a small city, or a neighborhood area, but not for a large city. Term J will also be kept.

Table B3
The terms in horizontal momentum equation for scale analysis.

	A	B	C	D	E	F
z-equation	$\frac{dw}{dt}$	$\frac{1}{\rho_0}\frac{\partial p'_h}{\partial h}$	g	$\mu_{eff}\frac{\partial^2 w_h}{\partial x^2}$	$\mu_{eff}\frac{\partial^2 w_h}{\partial y^2}$	$\mu_{eff}e^{-2\xi z}\frac{\partial^2 w_h}{\partial h^2}$
scales	$\frac{WU}{L}$	$\frac{R\delta T}{H}$	g	$\mu_{eff}\frac{W}{L^2}$	$\mu_{eff}\frac{W}{L^2}$	$\mu_{eff}e^{-2\xi H}\frac{W}{H^2}$
Using non-dimensional number	$\frac{U^3}{ND^2}$	$\frac{RN^2}{g\beta}$	g	$\frac{1}{Re}\frac{U^3}{ND^2}$	$\frac{1}{Re}\frac{U^3}{ND^2}$	$\frac{1}{Re}\frac{U^3}{ND^2}\frac{D^2}{H^2}$
Divided by $\frac{U^3}{ND^2}$	1	$\frac{RN^3D^2}{g\beta U^3}$	$\frac{g}{U}\frac{ND^2}{U^2}$	$\frac{1}{Re}$	$\frac{1}{Re}$	$\frac{1}{Re}\frac{D^2}{H^2}$
Order of the last row	10^0	10^6	10^6	10^{-9}	10^{-9}	10^{-7}
	G	H	I	J	K	L
z-equation	$\mu_{eff}\xi e^{-\xi z}\frac{\partial w_h}{\partial h}$	$\mu_{eff}\xi^2 w_h$	$\xi e^{\xi z}p'_h$	$\xi e^{\xi z}\rho_0 w_h^2$	$\rho_0\beta g(e^{2\xi z}-1)(T_h-T_0)$	$\rho_0 e^{\xi z}2\Omega u cos\varphi$
scales	$\mu_{eff}\xi\frac{W}{H}$	$\mu_{eff}\xi^2 W$	$\xi\rho_0 R\delta T$	$\xi\rho_0 W^2$	$\rho_0\beta g(e^{2\xi H}-1)\delta T$	$f_0 U$
Using non-dimensional number	$\xi\frac{1}{Re}\frac{U^3}{ND^2}\frac{D^2}{H}$	$\frac{1}{Re}\frac{U^3}{ND^2}D^2\xi^2$	$\xi\frac{\rho_0 RN^2 H}{g\beta}$	$\xi\rho_0\frac{U^4}{N^2D^2}$	$\rho_0 HN^2$	$f_0 U$
Divided by $\frac{U^3}{ND^2}$	$\xi\frac{1}{Re}\frac{D^2}{H}$	$\frac{1}{Re}D^2\xi^2$	$\xi\rho_0 H\frac{RN^3D^2}{g\beta U^3}$	$\xi\frac{\rho_0 U}{N}$	$\rho_0 HN^2\frac{ND^2}{U^2}$	$f_0\frac{ND^2}{U^2}$
Order of the last row	10^{-8}	10^{-9}	10^5	10^{-2}	10^5	10^2

Appendix C. Sensitive study for the simulation case.

A sensitive study usually focus on steady situation, while the two cases in Section 3 are all unsteady cases. Therefore, here we used the same mesh and settings as Section 3.1, but changed the situation to steady.

For the steady situation, all the computational domain in Fig. 5 is included, and a constant wind (1 m s^{-1}) comes from the left hand side and goes out from the right hand side. The heat flux released in the urban area is still 37 W m^{-2}. The original x dimension of the grid is 100 m (medium); it has been refined to 50 m (fine) and extend to 200 m (coarse) for the sensitivity study.

Fig. C1 shows the vertical velocity profile and the horizontal velocity profile at the center line of the domain, which is in the middle of the urban area in the three cases. The results show that the velocity difference between medium and fine gird is very small, and the medium grid is fine enough to capture the major characteristics of the simulation cases.
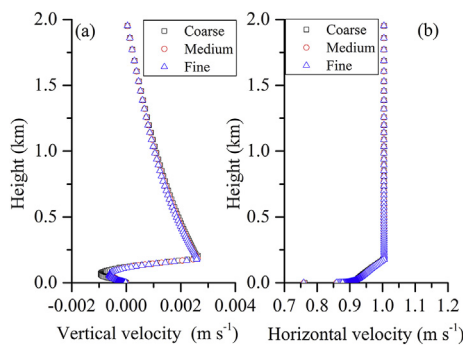

Fig. C1. Grid-sensitivity analysis using vertical profiles in the center of urban area for (a) vertical velocity and (b) horizontal velocity.

References

[1] Y. Ashie, T. Kono, Urban – scale CFD analysis in support of a climate-sensitive design for the Tokyo Bay area, Int. J. Climatol. 31 (2) (2011) 174–188.
[2] M. Balogh, G. Kristóf, Fine scale simulation of turbulent flows in urban canopy layers, Q. J. Hung. Meteorol. Serv. 114 (2010) 135–148.
[3] P.R. Bannon, J.M. Chagnon, R.P. James, Mass conservation and the anelastic approximation, Mon. Weather Rev. 134 (10) (2006) 2989–3005.
[4] B. Blocken, T. Stathopoulos, J. Carmeliet, J.L. Hensen, Application of computational fluid dynamics in building performance simulation for the outdoor environment: an overview, J. Build. Perform. Simul. 4 (2) (2011) 157–184.
[5] B. Blocken, 50 years of computational wind engineering: past, present and future, J. Wind Eng. Ind. Aerodyn. 129 (2014) 69–102.
[6] F. Catalano, A. Cenedese, S. Falasca, M. Moroni, Numerical and experimental simulations of local winds, in: National Security and Human Health Implications of Climate Change, Springer, Netherlands, 2012, pp. 199–218.
[7] M. Cavcar, The International Standard Atmosphere (ISA), Anadolu University, Turkey, 2000.
[8] O. Coceal, S. Belcher, A canopy model of mean winds through urban areas,, Q. J. R. Meteorol. Soc. 130 (2004) 1349–1372.
[9] T. Defraeye, B. Blocken, J. Carmeliet, CFD simulation of heat transfer at surfaces of bluff bodies in turbulent boundary layers: evaluation of a forced-convective temperature wall function for mixed convection, J. Wind Eng. Ind. Aerodyn. 104 (2012) 439–446.
[10] D.R. Durran, Improving the anelastic approximation, J. Atmos. Sci. 46 (11) (1989) 1453–1461.
[11] D.R. Durran, J.B. Klemp, A compressible model for the simulation of moist mountain waves, Mon. Weather Rev. 111 (12) (1983) 2341–2361.
[12] S. Emeis, Observational techniques to assist the coupling of CWE/CFD models and meso-scale meteorological models, J. Wind Eng. Ind. Aerodyn. 144 (2015) 24–30.
[15] R. Fuliotto, F. Cambuli, N. Mandas, N. Bacchin, G. Manara, Q. Chen, Experimental and numerical analysis of heat transfer and airflow on an interactive building facade, Energy Build. 42 (1) (2010) 23–28.
[16] T. Gál, J. Unger, Detection of ventilation paths using high-resolution roughness parameter mapping in a large urban area, Build. Environ. 44 (1) (2009) 198–206.
[17] G. Ganbat, J.-J. Baik, Y.-H. Ryu, A numerical study of the interactions of urban breeze circulation with mountain slope winds, Theor. Appl. Climatol. (2013) 1–13.
[18] C. Grimmond, T.R. Oke, .Aerodynamic properties of urban areas derived from analysis of surface form, J. Appl. Meteorol. 38 (1999) 1262–1292.
[19] R. Giridharan, S.S.Y. Lau, S. Ganesan, B. Givoni, Urban design factors influencing heat island intensity in high-rise high-density environments of Hong Kong, Build. Environ. 42 (10) (2007) 3669–3684.
[20] J. Hang, Y. Li, Wind conditions in idealized building clusters: macroscopic simulations using a porous turbulence model, Bound. Layer Meteorol. 136 (2010) 129–159.
[21] J. Hang, Y. Li, Macroscopic simulations of turbulent flows through high-rise building arrays using a porous turbulence model, Build. Environ. 49 (2012) 41–54.

[22] J.R. Holton, G.J. Hakim, An Introduction to Dynamic Meteorology, Academic Press, San Diego, 2013.

[23] A. Inagaki, M. Kanda, Turbulent organized structure over a reduced urban scale model-stability effect and horizontal distribution, in: Sixth Symposium on the Urban Environment, American Meteorological Society, 29 January-2 February 2006, Atlanta, GA, 2006.

[24] M.Z. Jacobson, Fundamentals of Atmospheric Modeling, Cambridge University Press, 2005.

[25] S. Kim, K. Yamaguchi, A. Kondo, S. Soda, A comparative study of the Mellor–Yamada and two-equation turbulence models in atmospheric application, J. Wind Eng. Ind. Aerodyn. 91 (2003) 791–806.

[26] G. Kristóf, N. Rácz, M. Balogh, Adaptation of pressure based CFD solvers for mesoscale atmospheric problems, Bound. Layer Meteorol. 131 (2009) 85–103.

[28] H. Kusaka, H. Kondo, Y. Kikegawa, F. Kimura, A simple single-layer urban canopy model for atmospheric models: comparison with multi-layer and slab models, Bound. Layer Meteorol. 101 (3) (2001) 329–358.

[29] B.E. Launder, D. Spalding, The numerical computation of turbulent flows, Comput. Methods Appl. Mech. Eng. 3 (1974) 269–289.

[30] D. Lilly, A comparison of incompressible, anelastic and Boussinesq dynamics, Atmos. Res. 40 (1996) 143–151.

[31] Y.L. Lin, Mesoscale Dynamics, Cambridge University Press, Cambridge, 2007.

[32] J. Lu, S.P. Arya, W.H. Snyder, R.E. Lawson Jr., A laboratory study of the urban heat island in a calm and stably stratified environment. Part II: velocity field, J. Appl. Meteorol. 36 (1997) 1392–1402.

[33] G.L. Mellor, T. Yamada, A hierarchy of turbulence closure models for planetary boundary layers, J. Atmos. Sci. 31 (1974) 1791–1806.

[34] A. Miettinen, T. Siikonen, Application of pressure-and density-based methods for different flow speeds, Int. J. Numer. Methods Fluids 79 (2015) 243–267.

[35] P.A. Mirzaei, F. Haghighat, Approaches to study urban heat island–abilities and limitations, Build. Environ. 45 (10) (2010) 2192–2201.

[36] A. Mochida, S. Iizuka, Y. Tominaga, I.Y.F. Lun, Up-scaling CWE models to include mesoscale meteorological influences, J. Wind Eng. Ind. Aerodyn. 99 (4) (2011) 187–198.

[37] D. Randall, The anelastic and Boussinesq approximations, Quick Stud. (2010).

[38] Y.H. Ryu, J.J. Baik, J.Y. Han, Daytime urban breeze circulation and its interaction with convective cells, Q. J. R. Meteorol. Soc. 139 (671) (2012) 401–413.

[39] C. Schär, D. Leuenberger, O. Fuhrer, D. Lüthi, C. Girard, A new terrain-following vertical coordinate formulation for atmospheric prediction models, Mon. Weather Rev. 130 (10) (2002) 2459–2480.

[40] K.H. Schlünzen, D. Grawe, S.I. Bohnenstengel, I. Schlüter, R. Koppmann, Joint modelling of obstacle induced and mesoscale changes − current limits and challenges, J. Wind Eng. Ind. Aerodyn. 99 (4) (2011) 217–225.

[41] W.C. Skamarock, J.B. Klemp, J. Dudhia, D.O. Gill, D.M. Barker, W. Wang, J.G. Powers, A Description of the Advanced Research WRF Version 2 (No. NCAR/TN-468+ STR), National Center for Atmospheric Research Boulder Co Mesoscale and Microscale Meteorology Div, 2005.

[42] M. Tewari, F. Chen, H. Kusaka, Implementation and evaluation of a single-layer urban canopy model in WRF/Noah, in: WRF Users' Workshop 2006, 2006.

[43] W. Wang, .The influence of thermally-induced mesoscale circulations on turbulence statistics over an idealized urban area under a zero background wind, Bound. Layer Meteorol. 131 (2009) 403–423.

[44] A.A. White, R.J. Beare, Flavours of pseudo-height, Q. J. R. Meteorol. Soc. 131 (606) (2005) 759–764.

[45] M.S. Wong, J.E. Nichol, P.H. To, J. Wang, A simple method for designation of urban ventilation corridors and its application to urban heat island analysis, Build. Environ. 45 (8) (2010) 1880–1889.

[46] WRF group, User's Guide for Advanced Research WRF (ARW) Modeling System Version 3.0, 2009.

[47] T. Yamada, Design Concept on Reduction of Heating and Air Pollution Concentrations in Urban Areas, American Meteorological Society, 2010.

[48] T. Yamada, K. Koike, Downscaling mesoscale meteorological models for computational wind engineering applications, J. Wind Eng. Ind. Aerodyn. 99 (4) (2011) 199–216.

[49] H. Yoshikado, Numerical study of the daytime urban effect and its interaction with the sea breeze, J. Appl. Meteorol. 31 (1992) 1146–1164.

[50] X. Yang, Y. Li, L. Yang, Predicting and understanding temporal 3D exterior surface temperature distribution in an ideal courtyard, Build. Environ. 57 (2012) 38–48.

[51] X. Yang, Y. Li, Development of a three-dimensional urban energy model for predicting and understanding surface temperature distribution, Bound. Layer Meteorol. 149 (2) (2013) 303–321.

[52] N. Zhang, X. Wang, Z. Peng, Large-Eddy Simulation of Mesoscale Circulations Forced by Inhomogeneous Urban Heat Island, Bound. Layer Meteorol. 151 (2014) 179–194.

[53] E. Ng, L. Chen, Y. Wang, C. Yuan, A study on the cooling effects of greening in a high-density city: an experience from Hong Kong, Building and Environment 47 (2012) 256–271.

[54] F. Scargiali, E. Di Rienzo, M. Ciofalo, F. Grisafi, A. Brucato, Heavy gas dispersion modelling over a topographically complex mesoscale: a CFD based approach, Process safety and environmental protection 83 (3) (2005) 242–256.